water

MDPI

Article

Numerical Simulation of Flow Fields and Sediment-Induced Wear in the Francis Turbine

Bing Xue [1,2], Yongbo Li [1,2], Youping Li [1,2], Zhengyang Tang [1,2], Bo Xu [1,2], Kang Xu [3], Ziyao Zhou [3], Zhishun Yu [3], Bing Yao [3], Jiayang Pang [3] and Xiaobing Liu [3,*]

[1] China Yangtze Power Co., Ltd., Yichang 443000, China
[2] Hubei Technology Innovation Center for Smart Hydropower, Wuhan 430010, China
[3] Key Laboratory of Fluid and Power Machinery, Ministry of Education, Xihua University, Chengdu 610039, China; xukang@stu.xhu.edu.cn (K.X.); pangjy@cau.edu.cn (J.P.)
* Correspondence: liuxb@mail.xhu.edu.cn

Abstract: Based on the solid–liquid two-phase flow model and the Realizable *k*-ε Turbulence model, numerical simulations of the sediment–water flow in the flow components of the turbine were conducted. The distribution of sediment-induced wear within the turbine was obtained by analyzing the sediment volume fraction (SVF) and the erosion rate. The results revealed that sediment-induced wear on the stay and guide vanes was primarily distributed along the water inlet edge of the stay and guide vanes. For the runner blades, wear was predominantly localized along the water inlet edge and near the lower ring. The sediment-induced wear patterns on these flow components were found to be consistent with the sediment volume fractions (SVFs) on their surfaces.

Keywords: Francis turbine; solid–liquid two-phase; sediment-induced wear; numerical simulation

check for updates

Citation: Xue, B.; Li, Y.; Li, Y.; Tang, Z.; Xu, B.; Xu, K.; Zhou, Z.; Yu, Z.; Yao, B.; Pang, J.; et al. Numerical Simulation of Flow Fields and Sediment-Induced Wear in the Francis Turbine. *Water* **2024**, *16*, 3148. https://doi.org/10.3390/w16213148

Academic Editor: Chin H Wu

Received: 29 September 2024
Revised: 23 October 2024
Accepted: 31 October 2024
Published: 4 November 2024

1. Introduction

Hydraulic turbines, as crucial components of hydropower systems, play a pivotal role in the global energy infrastructure. However, the increasing utilization of water resources has intensified sediment formation in rivers, posing severe threats to the secure and stable operations of these turbines. Sediment-induced wear, a major concern in hydraulic turbine operation, not only deteriorates the performance and efficiency of the equipment but also introduces serious stability risks. Consequently, thorough investigations on the sediment-induced wear of hydraulic turbines and explorations of effective protective measures for improving operational efficiency are essential. These efforts are critical for extending equipment lifespan and ensuring the safe operation of hydropower stations. E. Flores [1] et al. researched how a large Francis turbine can be engineered utilizing specific design methodologies, encompassing both global and local optimization techniques.

Currently, research on Francis turbines primarily relies on two methodologies: experimental investigations and numerical simulations. Pang [2] et al. employed the *k*-ε multiphase flow turbulence model to compute the sediment–water flow characteristics of a high-head Francis turbine, featuring both long and short blades, in the Minjiang River. Xiao-bing [3] developed a *k*-ε two-way turbulence model and volume fraction turbulence model of turbulent solid-liquid two-phase flows to numerically simulate flows and solid wall wear in the flow passages of water turbine machinery. Similarly, Pan [4] et al. utilized the Euler–Euler computational fluid dynamics (CFD) approach to simulate the steady liquid–solid two-phase flow in various pump and turbine operating modes. Furthermore, Jianfeng [5] et al. utilized a polyhedral mesh technique and the standard *k*-ε turbulence model to numerically simulate the two-phase turbulence field created by three-dimensional (3D) steady sediment-induced wear across the entire flow channel of a mixed flow turbine. They also analyzed the characteristic variation law of sediment-induced wear in the turbine flow channel. Jie [6] introduced a sediment phase based on clear water calculations and examined the influence of varying particle sizes and sediment concentrations on internal sediment-induced wear in hydraulic turbines. Lei [7] et al. developed a 3D water model of the complete flow channel of a Wanjiazhai prototype turbine, employing the discrete phase model (DPM) and the standard turbulence model to numerically simulate solid-liquid two-phase flows under four small-opening conditions. Using particle and heterogeneous models, Jie [8] et al. examined the effect of sediment particles on the performance of an axial flow pump and the wear characteristics of blades. Liu [9] et al. performed numerical simulations of the sediment–water flow within the injector of a large Pelton turbine, leveraging the solid–liquid two-phase flow model, the SST k-ε turbulence model, and the Lagrangian equation model for particle motion. Quan-you [10] et al. numerically simulated the internal flow field created by a two-phase flow containing sand across the full flow channel of a mixed-flow turbine under different opening conditions. They also analyzed the two-phase flow mechanism and sediment-induced wear characteristics of conventional runners, as well as those with long and short blades. In another study, Wang [11,12] et al. used the k-epsilon turbulence model, ZGB cavitation model, and sediment erosion prediction model to simulate the solid–liquid two-phase flow and cavitation of guide vane. Yanhao [13] et al. utilized the Mansouri wear model in conjunction with the Euler–Lagrange method to simulate the three-phase flow of sediment particles on the surface of the runner bucket. This analysis focused on examining the particle flow characteristics and wear distribution on the bucket surface under conditions of high sediment concentrations, which is typical during flood events. Jia [14] et al. alidated the efficacy of the Discrete Particle Model (DPM) in simulating the wear behavior of stay vanes and pinpointed the crucial areas susceptible to surface wear. Bing [15] et al. utilized the solid–liquid two-phase turbulence model alongside a sample algorithm to numerically simulate sand flow throughout the entire turbine channel. Wang [16] et al. employed particle model software and the non-uniform model within CFX to simulate a hydraulic turbine, with the objective of gaining insights into the wear and external characteristics of overflow components under solid–liquid two-phase flow conditions. Koirala [17] et al. investigated the impact of sediment erosion on the diversion blades at the Kaligandaki-A (KG-A) Hydropower Station, which is the largest operational hydropower facility in Nepal. Employing the volume of fluid multiphase flow model, Huang [18] et al. simulated the dynamics of three-phase (liquid–gas–solid) flows within the critical overflow component of an impactor turbine and made predictions regarding sediment-induced wear within the turbine. Utilizing the solid–liquid two-phase flow equation in conjunction with a turbulence model, Jun [19] et al. performed full-channel numerical simulations of water and sediment flows within a turbine and predicted the wear characteristics of its runner blades. Pang [20] et al. designed a flow-around wear test device tailored for the steering components of a reaction turbine, utilizing the principles of flow similarity and modifications in the velocity triangle. Lei [21] et al. employed the Euler–Euler two-phase flow model along with the renormalization group k-ε turbulence model to numerically simulate solid–liquid two-phase flows across various operational scenarios of a hydraulic turbine. This analysis evaluated the pressure, flow velocity, and sediment concentration within the guide vane area under the specified operating conditions. Han [22] et al. employed the solid-liquid two-phase standard k-ε turbulence model to numerically simulate the sand-water flow characteristics across the entire flow channel of a turbine, examining the wear condition of turbine guide vanes at the Xinjiang Xiate Power Station. Wang [23] et al. used the Lagrange method to examine the erosion characteristics of Francis turbines under varying water heads and accurately predicted sediment erosion during turbine operation by using the Tabakoff particle abrasion model. Rajan [24] et al. based on computational fluid dynamics (CFD) simulations and theoretical analyses, present the flow results for a draft tube of a model Francis turbine with constant head and constant specific velocity. Yang [25] et al. investigated the performance of a prototype high-head Francis turbine for heavy sediment power plants and analyzed the hydraulic performance, scour resistance characteristics, and cavitation performance by reducing the rotational speed and using a diverter runner. Xu [26] et al. employed Large-eddy Simulation (LES) as a turbulence modeling method to simulate three-dimensional (3D) non-stationary turbulence across the entire flow path of a Francis turbine. This enabled them to obtain flow conditions in various parts of the turbine under varying operating conditions. Their study identified the factors impacting turbine stability and delved into the formation mechanisms and evolution laws associated with these factors.

However, the sediment abrasion characteristics of Francis turbines under different load conditions have not been fully investigated. To further expand this aspect, this study numerically simulates the Francis turbine under varying working conditions and determines the SVFs on the turbine's flow components. The aim of this study is to analyze the sediment-induced wear of different turbine components, providing a reference for future research on the effects of sediments on the Francis turbine.

2. Mathematical Model

2.1. Basic Control Equations for Fluid Motion

Continuity equation:

$$\frac{\partial \rho}{\partial t} + \frac{\partial}{\partial x_i}(\rho V_i) = 0 \tag{1}$$

Equation of motion (N-S equation):

$$\frac{\partial}{\partial t}(\rho V_i) + \frac{\partial}{\partial x_i}(\rho V_i V_j) = \frac{\partial \tau_{ij}}{\partial x_i} + \rho g_i \tag{2}$$

Including the following:

$$\tau_{ij} = \mu\left(\frac{\partial V_i}{\partial x_j} + \frac{\partial V_j}{\partial x_i}\right) - \left(P + \frac{2}{3}\mu\frac{\partial V_k}{\partial x_k}\right)\delta_{ij}, \delta_{ij} = \begin{cases} 1 & j = i \\ 0 & j \neq i \end{cases}$$

where t is time, V is the fluid velocity, ρ is the fluid density, P is the pressure, μ is the hydrodynamic viscosity coefficient, g is the gravitational acceleration, and x is the coordinate. The subscripts i, j, and k are the tensor coordinates [27].

2.2. Turbulence Model

The Realizable k-ε Turbulence model is well suited for simulating complex shear flows that involve rapid deformation, slight rotation, vortices, and local transitional flows. Therefore, this article chooses the Realizable k-ε model [28].

Turbulence kinetic energy k equation:

$$\frac{\partial(pk)}{\partial t} + \frac{\partial(pkV_i)}{\partial x_i} = \frac{\partial}{\partial x_j}\left[\left(\mu + \frac{\mu_t}{\sigma_k}\right)\frac{\partial k}{\partial x_j}\right] + G_k - \rho\varepsilon \tag{3}$$

Turbulent kinetic energy dissipation rate ε equation:

$$\frac{\partial}{\partial t}(\rho\varepsilon) + \frac{\partial}{\partial x_i}(\rho\varepsilon V_i) = \frac{\partial}{\partial x_j}\left[\left(\mu + \frac{\mu_t}{\sigma_\varepsilon}\right)\frac{\partial \varepsilon}{\partial x_j}\right] + \rho C_1 S\varepsilon - \rho C_2\frac{\varepsilon^2}{K + \sqrt{\nu\varepsilon}} \tag{4}$$

where $C_1 = \max\left[0.43, \frac{\eta}{\eta+5}\right], \eta = S\frac{k}{\varepsilon}, C_2 = 1.9, \sigma_k = 1.0, \sigma_\varepsilon = 1.2, S = \sqrt{2S_{ij}S_{if}}, S_{if} = \frac{1}{2}\left(\frac{\partial V_i}{\partial x_i} + \frac{\partial V_j}{\partial x_j}\right)$, ρ is the gas–fluid density, V is the fluid velocity, and μ, μ_t are the viscosity coefficients of laminar flow and turbulent flow, respectively. G_K is the turbulent kinetic energy due to the mean velocity gradient, G_b is the turbulent kinetic energy due to buoyancy, Y_M is the contribution to the dissipation rate due to diffusion of the transitions, and S_f, S_p, S_k, S_ε are the source terms of the definition. k is the turbulence kinetic energy, ε is the turbulent kinetic energy dissipation rate, S_{ij} is the time-averaged strain rate tensor, η is the efficiency, and σ is the cavitation coefficient [29].

2.3. Wear Model

When the sediment impacts the turbine overflow components, it causes the turbine overflow components to be subjected to cutting-type erosion. In this erosion process, the contact between the sediment particles and the surface of the turbine overflow component is strongly influenced by the characteristics of the sediment particles themselves and the nature of the solid surface. The erosion rate is a combination of factors closely related to the type of wall material, the composition of the deposit, the velocity of the deposit, and the impact velocity at the time of impact.

This article uses the generic wear model. Compared to specific wear models such as Finnie, McLaury, Oka, etc., which are based on specific experimental conditions, this model can adjust relevant parameters independently to better reflect the actual wear situation [30]. The generic model was employed to predict both the distribution and the severity of erosion on the turbine, which is defined as follows:

$$R_{erosion} = \sum_{p=1}^{N_{porticles}} \frac{\dot{m}_p C(d_p) f(\alpha) \mathrm{v}^{b(\mathrm{v})}}{A_{face}} \tag{5}$$

where R_e is the erosion rate, N_p is the total number of particles, m_p is the particle mass flow rate, $C(d_p)$ is the particle size function, $f(\alpha)$ is the impact angle function (α is the angle at which the particles impact the wall), $b(v)$ is the function of the relative velocity of the particles (v is the relative velocity of the particles to the wall), and A_{face} is the wall area (m^2). The erosion model parameters were set as follows. The normal bounce coefficient was defined as [31]:

$$\varepsilon_N = 0.993 - 0.0307\alpha + 4.75 \times 10^{-4}\alpha^2 - 2.61 \times 10^{-6}\alpha^3 \tag{6}$$

The tangential bounce coefficient was defined as

$$\varepsilon_T = 0.998 - 0.029\alpha + 6.43 \times 10^{-4}\alpha^2 - 3.56 \times 10^{-6}\alpha^3 \tag{7}$$

The impact angle function was defined in a segmented linear way. The particle size function was set to 1.8×10^{-9}, and the velocity index function was set to 2.6.

3. Computational Domain and Meshing

3.1. Computational Domain

The runner of the Francis turbine features a shunt vane design, comprising 15 long vanes and 15 shunt (short) vanes. Notably, the leading edge profiles of the long and shunt vanes are similar. The blades can twist up to 180° along the chord from the inlet to the outlet of the flow channel, with a trailing edge thickness of approximately 3 mm. The inlet and outlet diameters of the flow channel are 0.630 and 0.349 m, respectively. Figure 1 illustrates the established 3D computational domain model of the Francis turbine, while Table 1 details the relevant parameters of the turbine model.

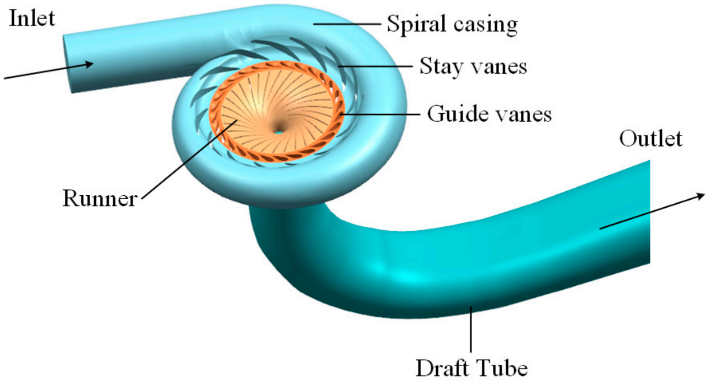

Figure 1. Three-dimensional model diagram of the Francis turbine.

Table 1. Basic parameters of the Francis turbine.

Parameter	Value	Parameter	Value
Operating head (m)	12.0	Stay vane	14
Runner inlet diameter (m)	0.630	Guide vane	28
Runner outlet diameter (m)	0.349	Runner blade (long + short)	15 + 15
Hydraulic efficiency (%)	92.4		

3.2. Grid Partitioning and Independence Verification

Given the importance of efficiency in hydraulic machinery operations, a hexahedral unstructured mesh was employed for the entire flow channel. Five sets of grid schemes were considered, with grid counts ranging from 9.8×10^6 to 8.75×10^6. Grid independence was evaluated using unit efficiency as the reference value. Ultimately, the fifth set of grids, comprising 8.75×10^6 grids, was selected as the optimal configuration, as detailed in Table 2. The grid diagram of the model is shown in Figure 2.

Table 2. Grid independence verification results.

Grid Scheme	Number of Grids ($\times 10^4$)	Simulation Efficiency (%)	Actual Efficiency (%)
1	98	92.6	93.0
2	204	92.3	93.0
3	395	92.4	93.0
4	603	92.8	93.0
5	875	95.7	93.0

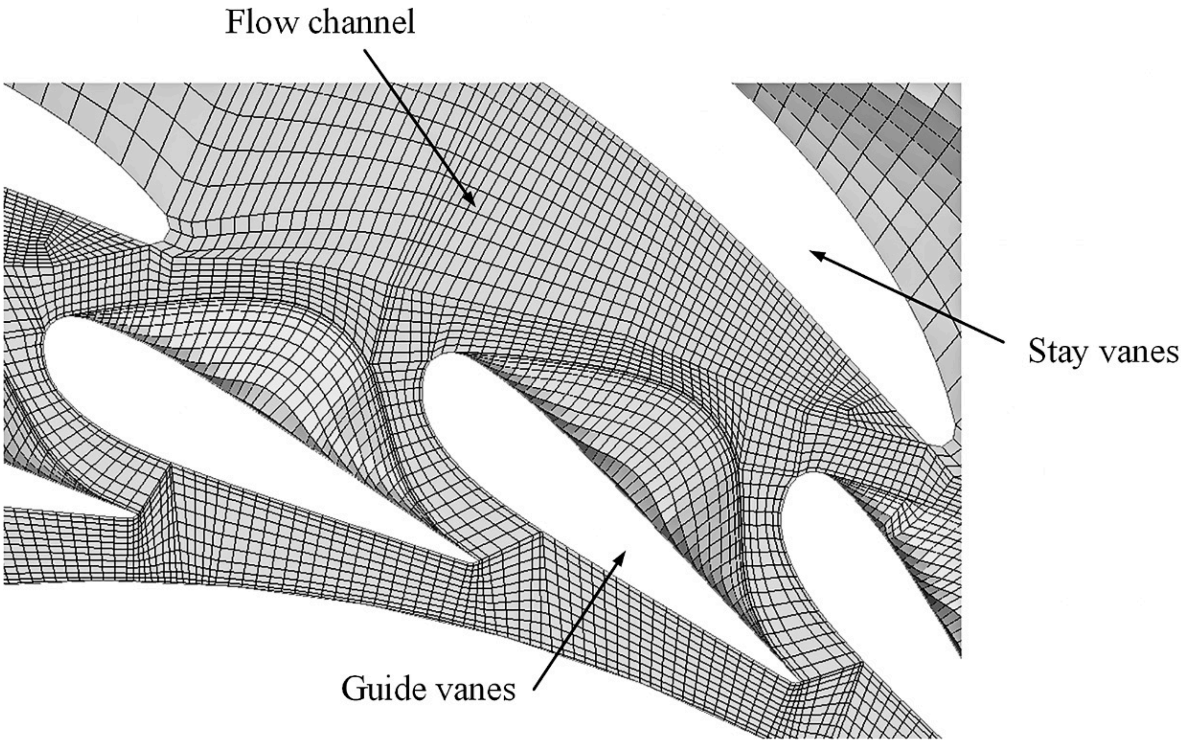

Figure 2. Component grid diagram of the Francis turbine.

3.3. Boundary Conditions

Our calculations considered three operating conditions: low load, design load, and heavy load. For turbines utilizing incompressible fluids as their medium, boundary conditions include the following: flow (velocity and pressure) inlet boundary, flow (velocity and pressure) outlet boundary, wall boundary, and periodic boundary. The inlet boundary condition is specified as a velocity inlet, while the outlet boundary condition is defined as a pressure outlet. The specific values of the boundary conditions under the three working scenarios are listed in Table 3.

Table 3. Boundary conditions across the examined operating scenarios.

Parameter	Low-Load Condition	Design Load Condition	Heavy-Load Condition
Flow rate (m^3/s)	0.07	0.20	0.22
Guide vane angle (°)	3.91	9.84	12.44
Runner speed (rpm)	406.2	344.4	380.4
Velocity inlet (m/s)	0.814	2.328	2.534
Pressure outlet (Pa)	99,540	101,560	95,980

For the sediment phase, the median particle size was set to 0.27 mm, while the sediment concentration was set to 2.5 kg/m^3.

4. Result Analysis

4.1. Wear Analysis of Stay Vane

As shown in Figure 3, under the three load conditions, the sediment distribution in the region of the volute and the stay vane is uneven, and the sediment accumulation area gradually increases along the flow direction of the volute. Under the influence of centrifugal force, the volume fraction of sediment near the outer wall of the volute is larger. Under the design load condition and heavy-load condition, the sediment is affected by the flow and centrifugal force and accumulates in the nose area of the volute, resulting in a larger SVF near the nose. Under the low-load condition, the influence of gravity on sediment increases due to the small discharge, and the sediment mainly accumulates in the R4 region. The SVF above 0.00108 is mainly concentrated in the R4 area under small flow conditions, the R1 and R2 areas under design flow conditions, and the R1 and R2 areas under large flow conditions.

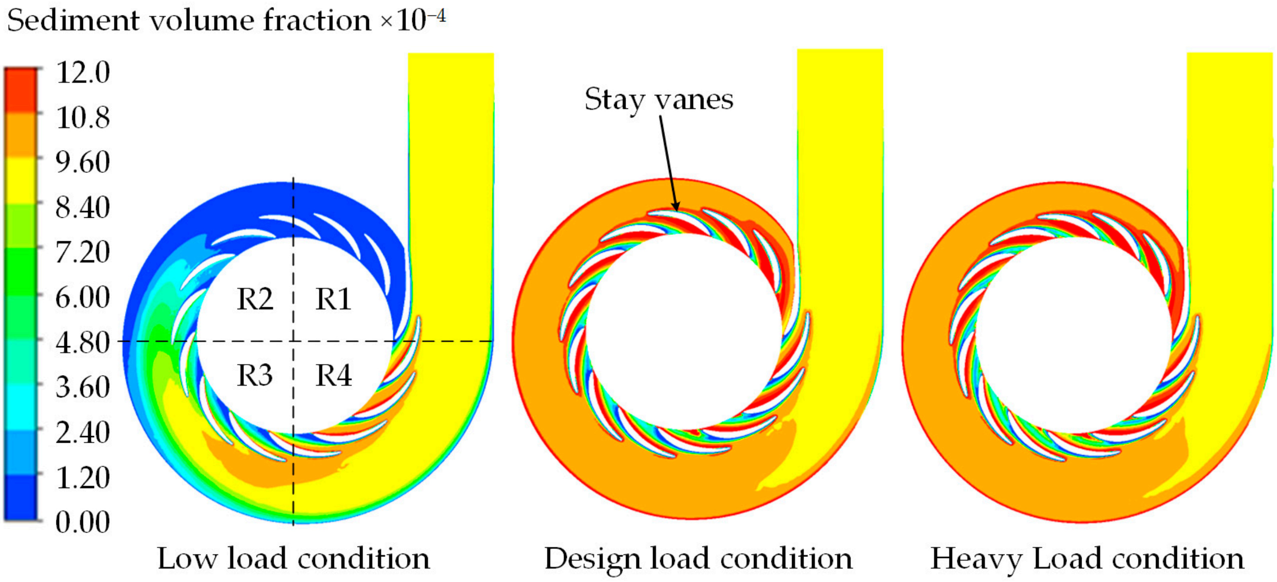

Figure 3. SVF in the spiral casing and stay vane at 50% leaf height.

The tail height of the stay vane serves as the benchmark for the 10% and 50% blade heights. As illustrated in Figures 4 and 5, the sediment distributions on the surface of the stay vane are generally similar across the three operating conditions. Specifically, sediment is predominantly located in the tail area, the bottom area at the front of the stay vane, and the bottom area at the back of the stay vane. Under the low-load condition, SVFs exceeding 0.0072 primarily appear in the bottom regions at the front and back of the stay vane, with almost no sediment distribution at the top of the stay vane. The sediment distributions under the design and heavy-load conditions closely resemble each other, with SVFs exceeding 0.0072 predominantly appearing in the front and rear regions, as well as the bottom regions at the back of the stay vane. Under low-load conditions, in view of the slowing down of the flow velocity and the relatively large diameter of the particles (d = 0.27 mm), the influence of natural forces such as gravity on the sediment particles becomes more significant, prompting the sediment particles to undergo the spontaneous settling process, resulting in the area where the SVF is more than 0.0072, which occurs mainly at the bottom of the back side of the stay vane.

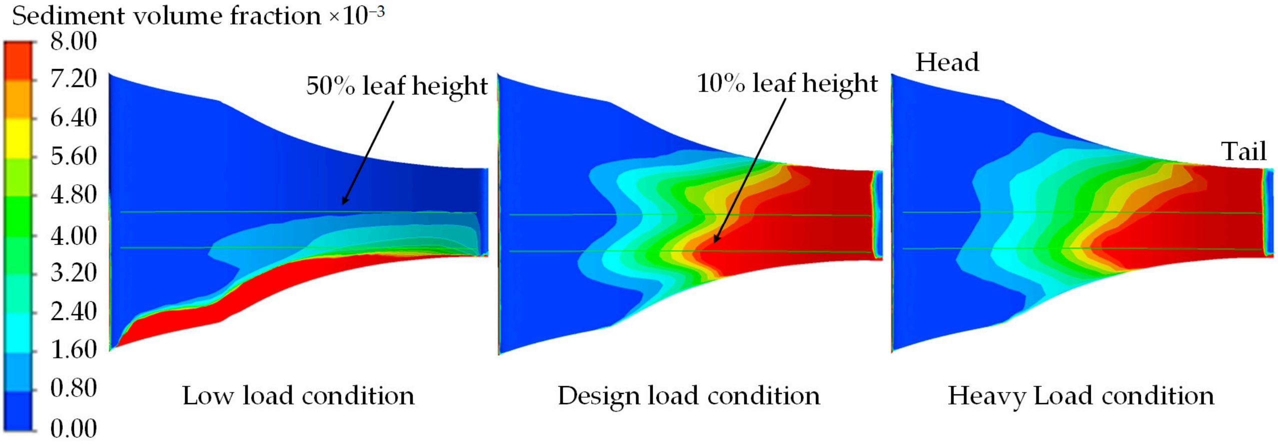

Figure 4. SVF at the front of the stay vane.

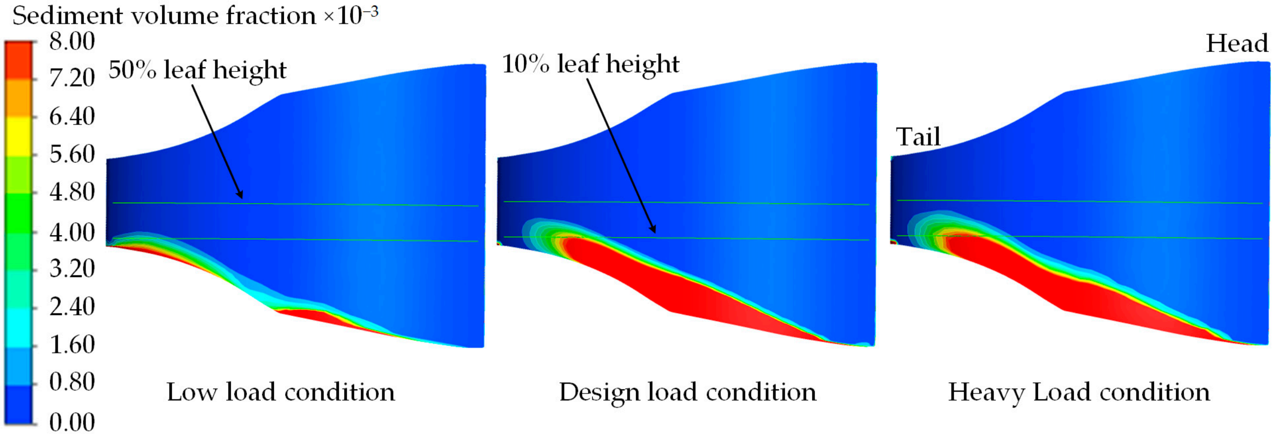

Figure 5. SVF at the back of the stay vane.

Figures 6 and 7 illustrate the SVF curves on the surface of the guide vane at 10% and 50% blade heights. Under all three working conditions, the SVFs at the front and back of the stay vane initially decrease, then increase, and subsequently decrease again from the head to the tail. Notably, the SVF at the front of the guide vane in the tail region exceeds that at the back. The maximum SVFs observed on the surface of the guide vane are approximately 0.0111, 0.0224, and 0.0237 under the low-load, design load, and heavy-load conditions, respectively. The peak values and trends of the SVF curves on the surface of the stay vane at 10% and 50% blade heights are similar under both the design load and heavy-load conditions. Conversely, the low-load condition exhibits a different curve owing to the lower flow rate and the more substantial influence of gravitational forces.

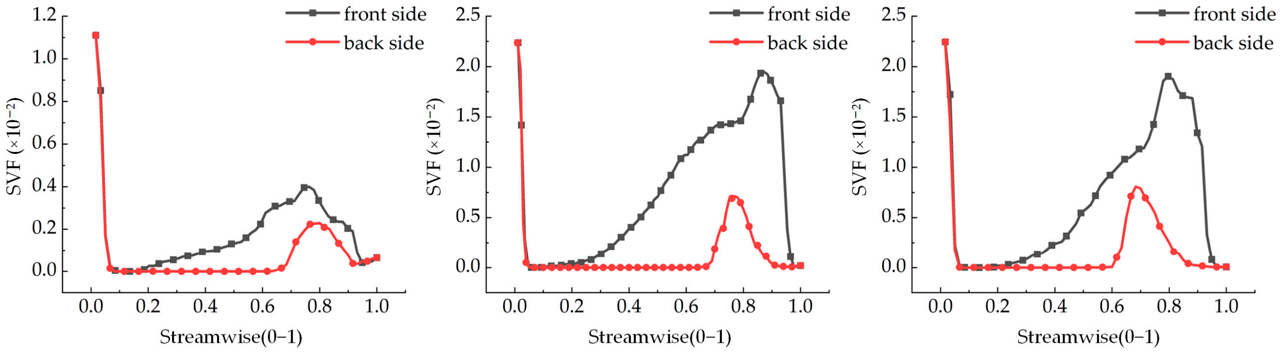

Low load condition Design load condition Heavy load condition

Figure 6. SVF on the stay vane surface at 10% blade height.

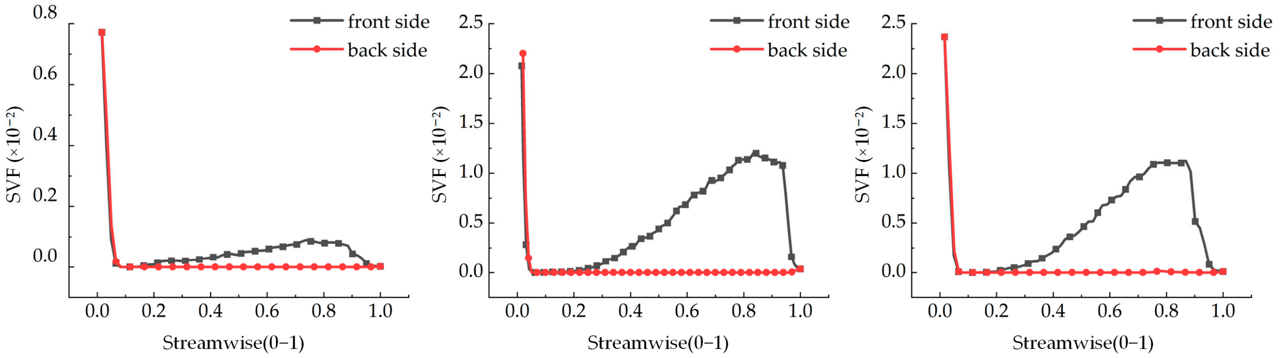

Low load condition Design load condition Heavy load condition

Figure 7. SVF on the stay vane surface at 50% blade height.

As illustrated in Figures 8 and 9, the surface sediment-induced wear distribution on the stay vane is minimal across all three working conditions and is predominantly concentrated in the head region. Under low-load conditions, the front and back surfaces of the stay vane exhibit almost no signs of wear. Conversely, under the design load and heavy-load conditions, sediment-induced wear appears in the head and bottom regions of the guide vane; however, the extent of this wear remains small in both cases. The degree of sediment-induced wear on the front and back surfaces of the guide blade increases with increasing flow rate. Overall, sediment-induced wear on the surfaces of the guide blade remains minimal across the three working conditions, with most regions exhibiting the erosion rate ranging from 2.0×10^{-8} $kg \cdot s^{-1}m^{-2}$ to 4.0×10^{-8} $kg \cdot s^{-1}m^{-2}$. Only a few regions exhibit an erosion rate exceeding 8.0×10^{-8} $kg \cdot s^{-1}m^{-2}$.

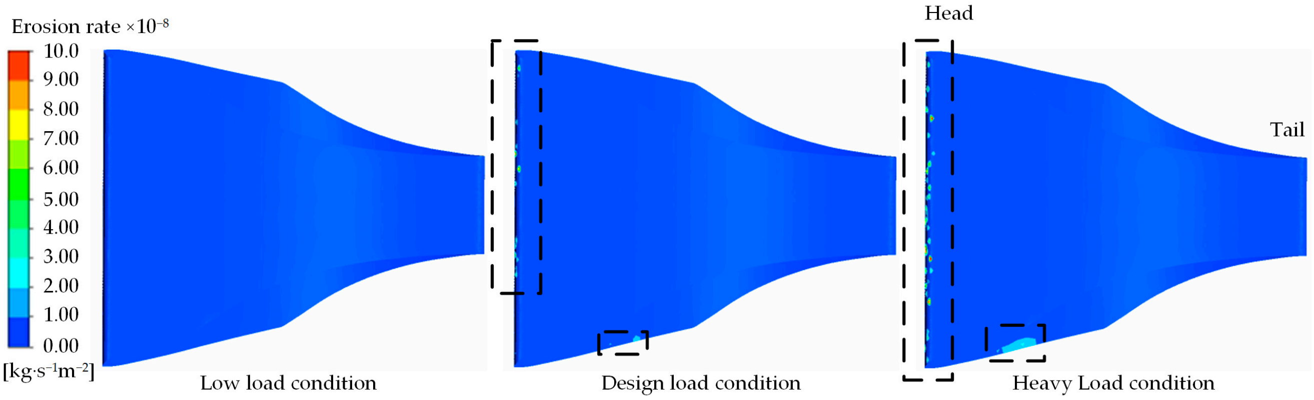

Low load condition Design load condition Heavy Load condition

Figure 8. Sediment-induced wear distribution at the front of the stay vane.

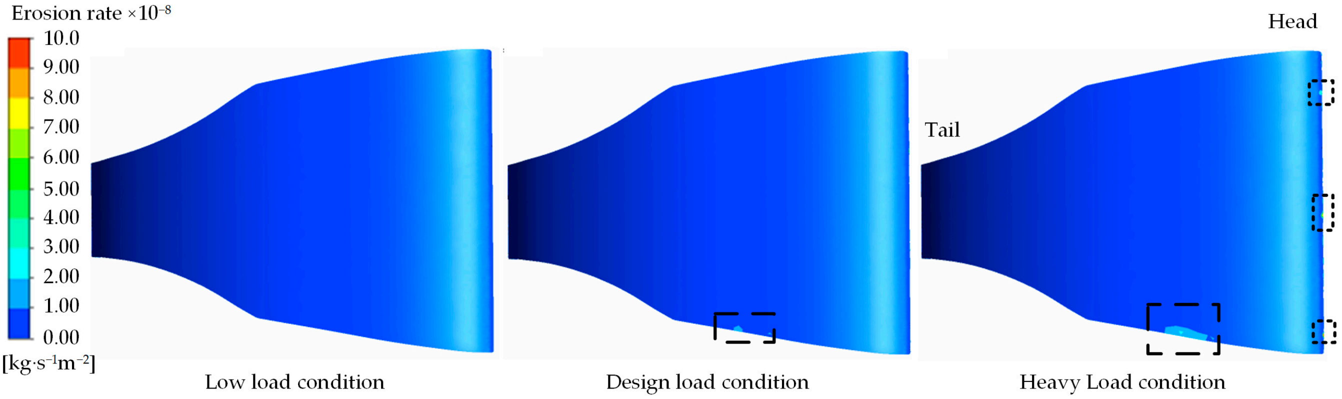

Figure 9. Sediment-induced wear distribution at the back of the stay vane.

4.2. Wear Analysis of the Guide Vane

As illustrated in Figure 10, under all three working conditions, the sediment distribution at 50% of the height of the movable guide blade is circular but not entirely symmetrical. In particular, under the low-load condition, the SVF is relatively small (ranging from 0.0008 to 0.0014) and is primarily concentrated in the R4 region at 50% of the height of the guide vane. Owing to the low flow rate, the SVFs in the R1, R2, and R3 regions remain minimal. Conversely, under the design load and heavy-load conditions, the sediment distribution is similar and considerably higher than that observed under the low-load condition. The area with SVFs exceeding 0.0018 is evenly distributed in a circular pattern, with notable sediment accumulation occurring at the interface between the R3 and R4 regions at 50% height of the guide vane.

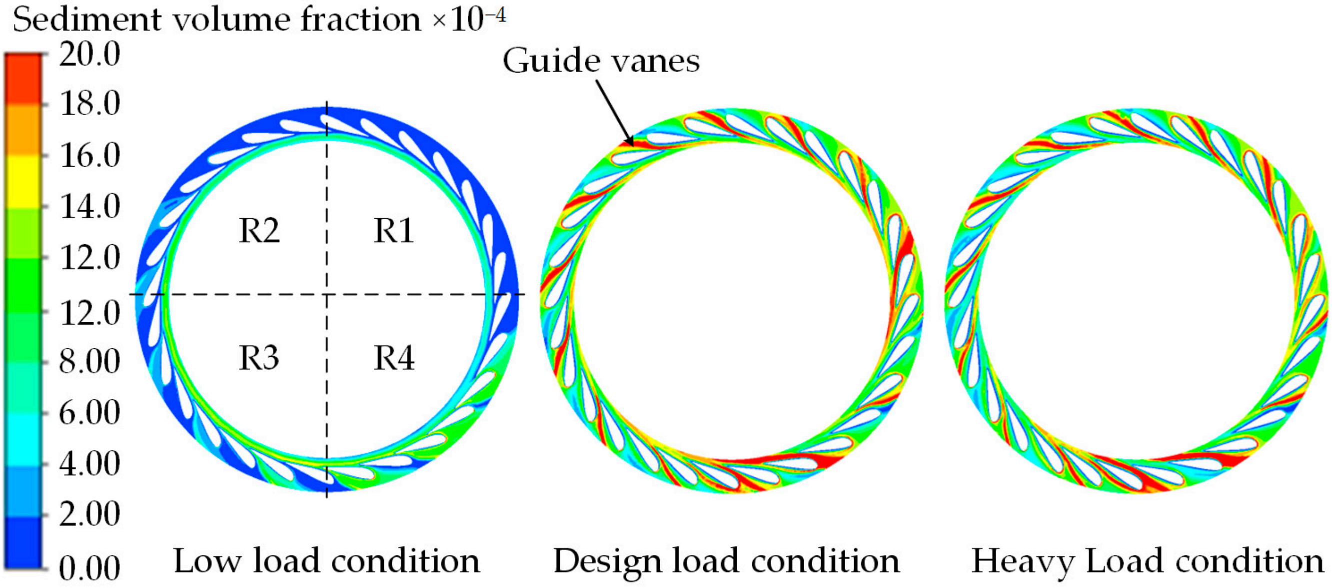

Figure 10. SVF at 50% of the leaf height of the guide vane.

Figures 11 and 12 further demonstrate that under the three working conditions, the SVF distribution remains similar at the front and back of the guide vane. Sediment primarily accumulates in the head region at the front and back of the guide vane, with the distribution area at the front considerably surpassing that at the back. Under the low-load condition, areas with SVFs exceeding 0.00009 are primarily concentrated at the front and bottom of the guide vane, where the sediment distribution is substantially influenced by gravity owing to the lower flow rate. Under the design load and heavy-load conditions, the sediment distribution remains roughly similar, with areas having SVFs greater than 0.00009 being primarily localized in the head region of the guide vane, near the disk and bottom edge. On the back of the guide vane, sediment is primarily concentrated in the middle portion of the guide vane head. Under low-load conditions, due to the slowing down of the flow velocity and the relatively large particle size (d = 0.27 mm), the influence of gravity and other natural factors on the sediment particles becomes more significant, prompting the sediment particles to undergo a natural settling process, resulting in the area where the SVF is greater than 0.0072, which mainly occurs at the bottom of the back side of the guide vane.

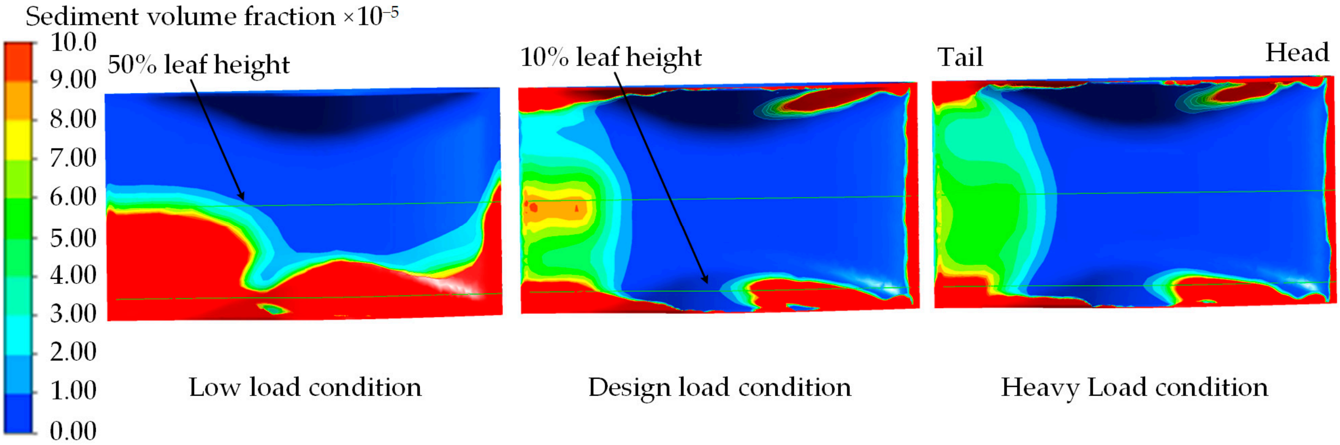

Figure 11. SVF at the front of the guide vane.

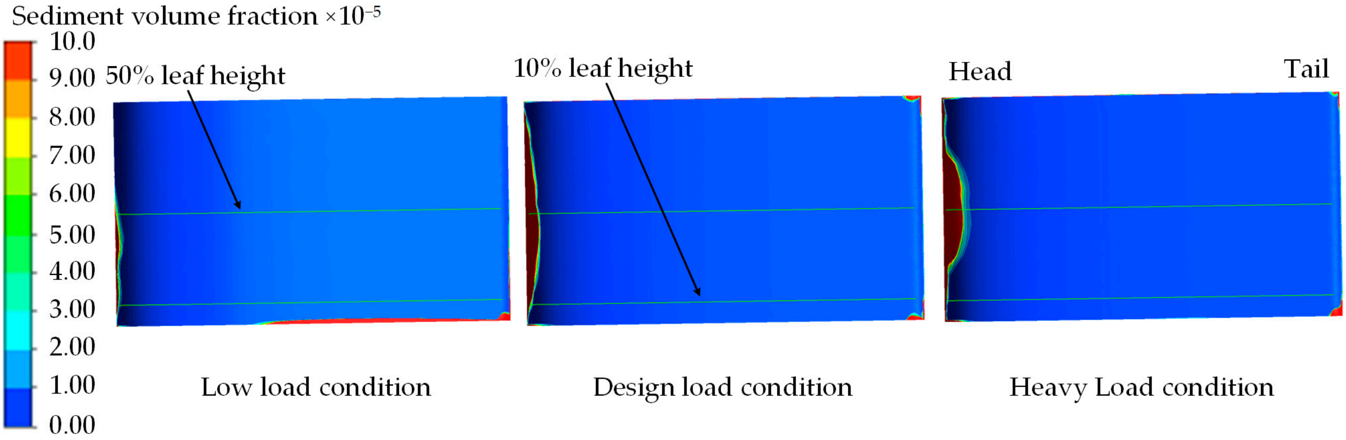

Figure 12. SVF at the back of the guide vane.

Figures 13 and 14 illustrate the SVF curves on the surface of the guide vane at 10% and 50% blade heights. Across all three working conditions, the SVF at the front of the guide vane exceeds that at the back, while the remainder of the vane experiences relatively low sediment accumulation. The maximum SVF on the surface of the guide vane is approximately 0.00933, 0.0214, and 0.0115 under low-load, design load, and heavy-load conditions, respectively. Under the low-load condition, the SVF on the front of the guide vane at 10% height initially decreases, increases, decreases again, and, finally, increases from the head to the tail, reaching its peak in the head region of the guide vane. The peak values and variation trends of the SVF on the stay vane surface at 10% and 50% blade heights are identical under the design and heavy-load conditions, with the maximum SVF again occurring in the head area of the guide vane.

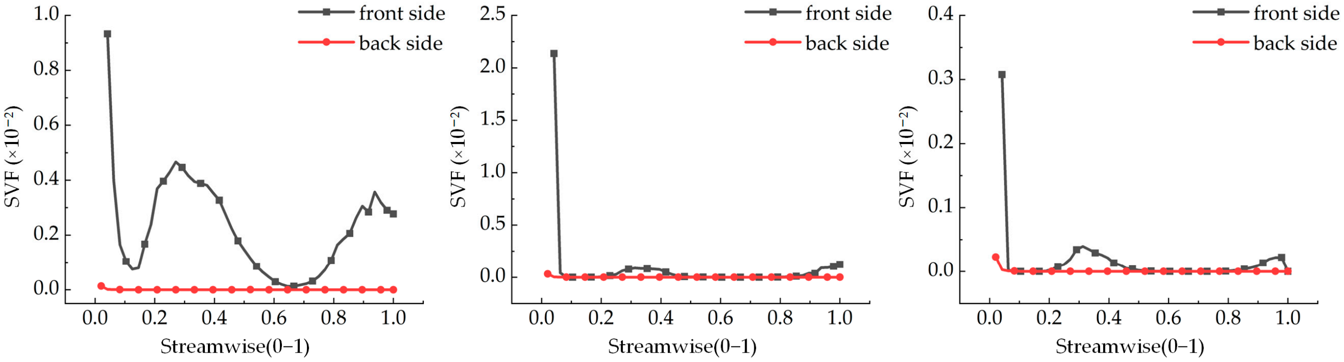

Low load condition Design load condition Heavy load condition

Figure 13. SVF on the surface of the guide vane at 10% blade height.

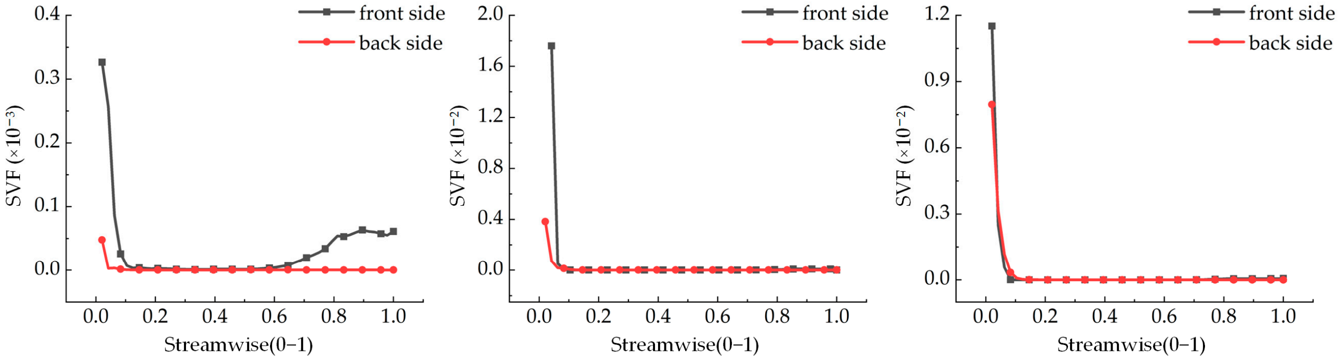

Low load condition Design load condition Heavy load condition

Figure 14. SVF on the surface of the guide vane at 50% blade height.

As illustrated in Figures 15 and 16, sediment-induced wear on the surface of the guide vane is primarily concentrated in the head region across all three working conditions. The extent of this sediment-induced wear on the guide vane surface increases with increasing flow rate. Under the design and heavy-load conditions, the impact of sediment on the head of the guide vane leads to substantial wear in that area. Regions with sediment-induced erosion rate exceeding 9.0×10^{-8} kg·s^{-1}m^{-2} are primarily localized in the head area of the guide vane, while the remainder of the guide vane exhibits minimal wear. Under the low-load condition, the wear in the head region of the guide vane is negligible owing to the lower flow rate, while the erosion rate in the tail region exceeds 9.0×10^{-8} kg·s^{-1}m^{-2}, with almost no wear observed at the back of the guide vane.

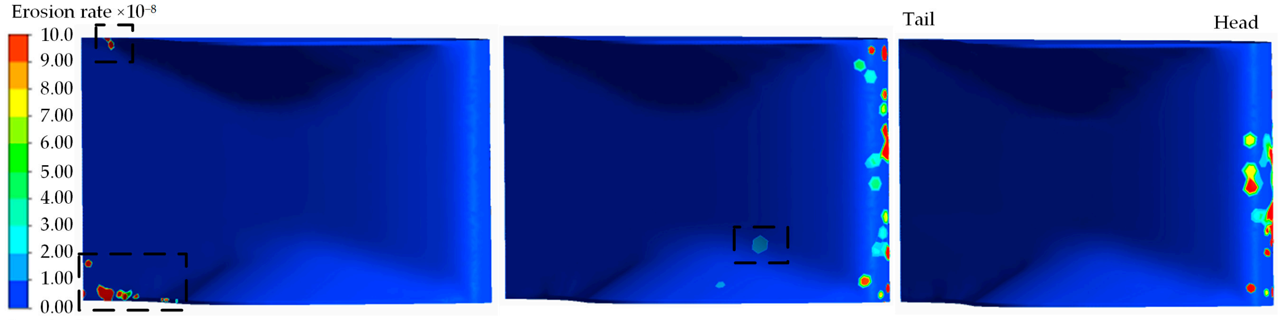

Low load condition Design load condition Heavy Load condition

Figure 15. Sediment-induced wear distribution at the front of the guide vane.

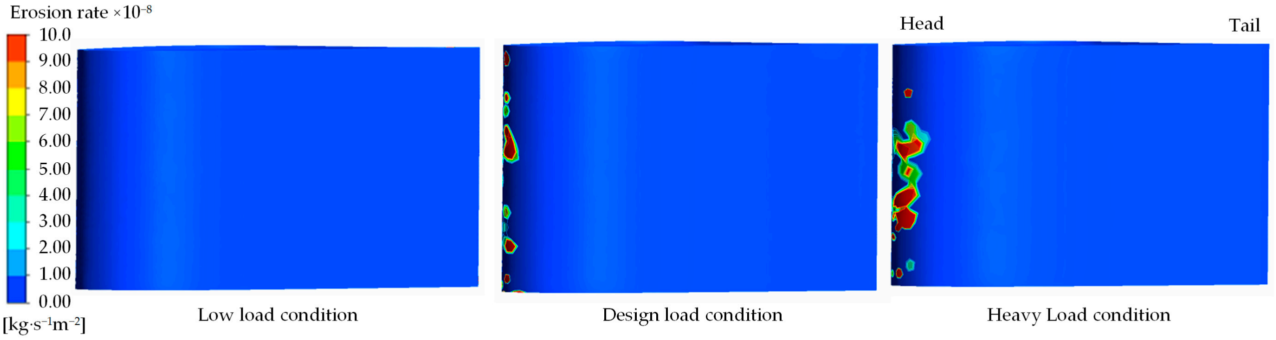

Figure 16. Sediment-induced wear distribution at the back of the guide vane.

4.3. *Wear Analysis of the Runner Blades*

(1) Analysis of the runner's long blade

Figures 17 and 18 illustrate sediment distribution on the runner's long blade under the three working conditions. As depicted, sediment tends to accumulate near the water outlet and is concentrated in specific regions. Under low-load conditions, the front surface of the runner's long blade presents almost no sediment deposition. Areas with SVFs exceeding 0.0018 are primarily concentrated in the middle section of the back side of the long blade and near the lower ring at the water outlet. Under both the design load and heavy-load conditions, the sediment distribution on the surface of the runner's long blade remains consistent, with almost no sediment deposition on the back surface of the blade. Areas with SVFs exceeding 0.0018 are predominantly concentrated along the water edge at the front of the long blade. Under heavy-load conditions, sediment deposition is observed at the bottom of the back side of the long blade near the lower ring.

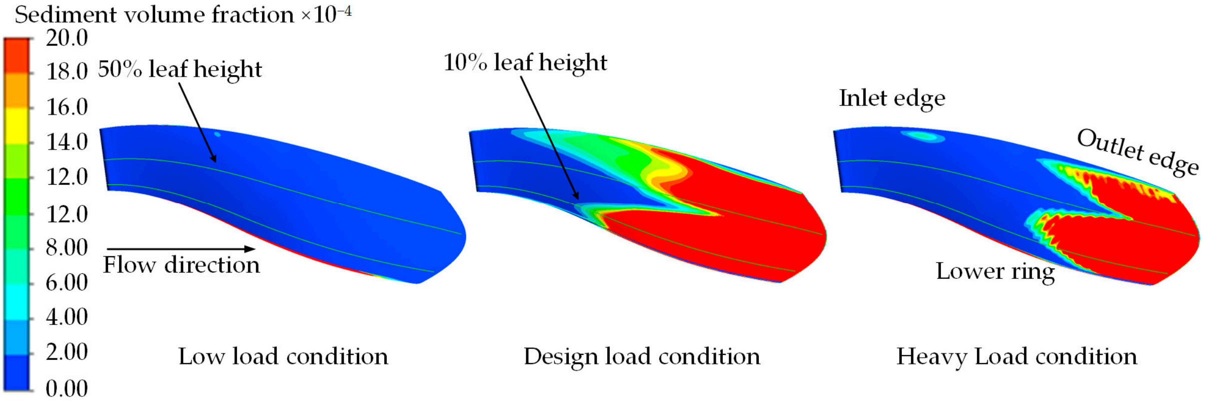

Figure 17. SVF at the front of the runner's long blade.

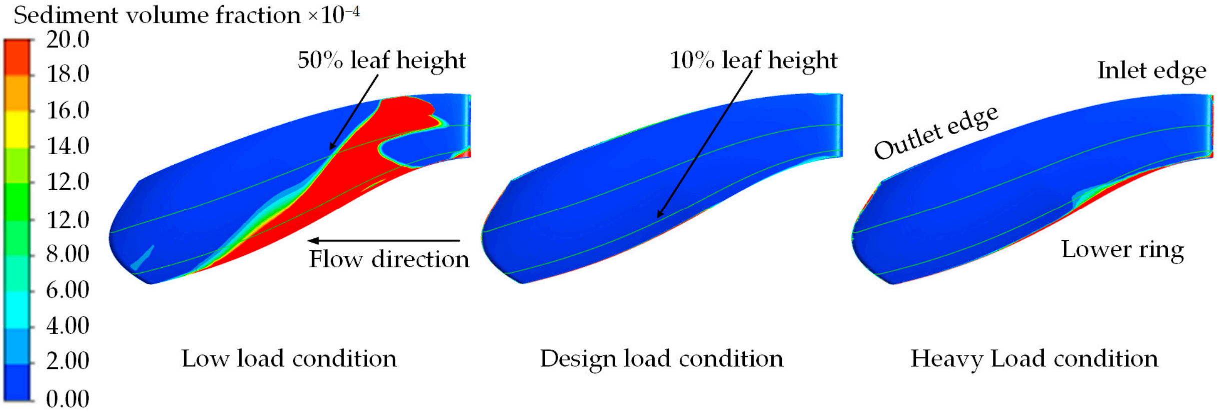

Figure 18. SVF at the back of the runner's long blade.

Figures 19 and 20 illustrate the SVF curves on the surface of the active guide blade at 10% and 50% blade heights. Under the low-load condition, almost no sediment deposition is observed on the front side of the runner's long blade, while the SVF on the back side initially increases and subsequently decreases from the water inlet edge to the water outlet edge. The maximum SVF on the blade surface reaches approximately 0.2785. Under both the design load and heavy-load conditions, the sediment distribution on the surface of the runner's long blade remains similar, with minimal sediment deposition at the back of the runner's long blade. The SVF at the front of the blade exhibits a gradual decline from the water inlet edge to the water outlet edge. At the 10% height, the SVF experiences a steep decline, while at the 50% blade height, the decline is more gradual. The maximum SVF on the surface of the blade is approximately 0.0212 and 0.0203 under the design and heavy-load conditions, respectively.

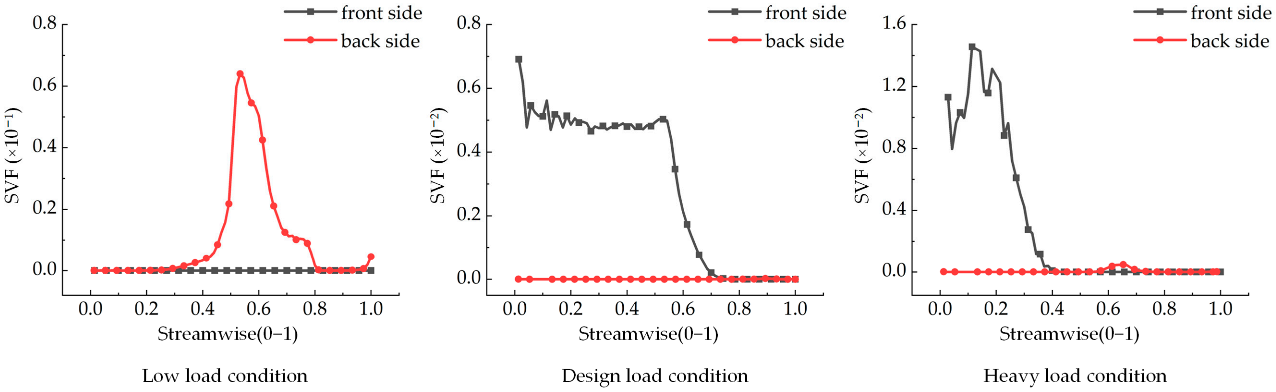

Figure 19. SVF on the surface of the runner's long blade at 10% blade height.

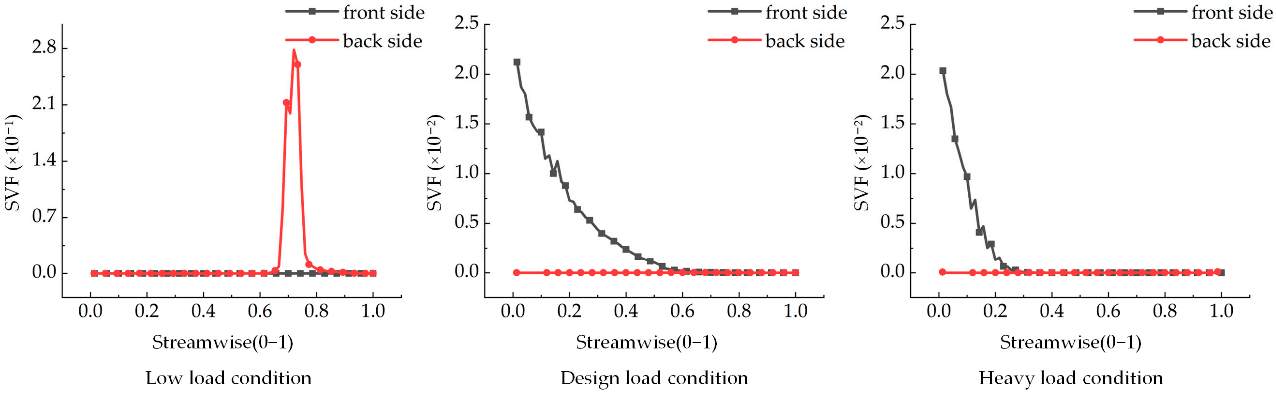

Figure 20. SVF on the surface of the runner's long blade at 50% blade height.

As illustrated in Figures 21 and 22, sediment-induced wear on the surface of the runner's long blade is minimal across all three working conditions. This wear is primarily concentrated along the water outlet edge and near the lower ring. Under the low-load condition, only the front side of the runner's long blade, near the water inlet, experiences slight sediment-induced wear, while the back exhibits wear primarily in the area near the bottom ring. Regions with an erosion rate exceeding 8.0 × 10^{-8} kg·$s^{-1}m^{-2}$ are primarily localized at the edge of the lower ring of the runner's long blade. Under the heavy-load condition, minimal sediment-induced wear appears at the back of the runner's long blade, while the wear distribution at the front is wider and more granular and is primarily concentrated at the bottom of the blade near the lower ring area. Under the design load condition, the back of the runner's long blade exhibits no sediment-induced wear, and only slight wear is observed at the front, primarily along the water edge of the blade. Under this condition, the erosion rate on the surface of the long blade ranges from 3.0 × 10^{-8}

to 8.0 × 10^{-8} kg·$s^{-1}m^{-2}$, lower than those observed under the low-load and heavy-load conditions, owing to less pronounced influence from sand currents.

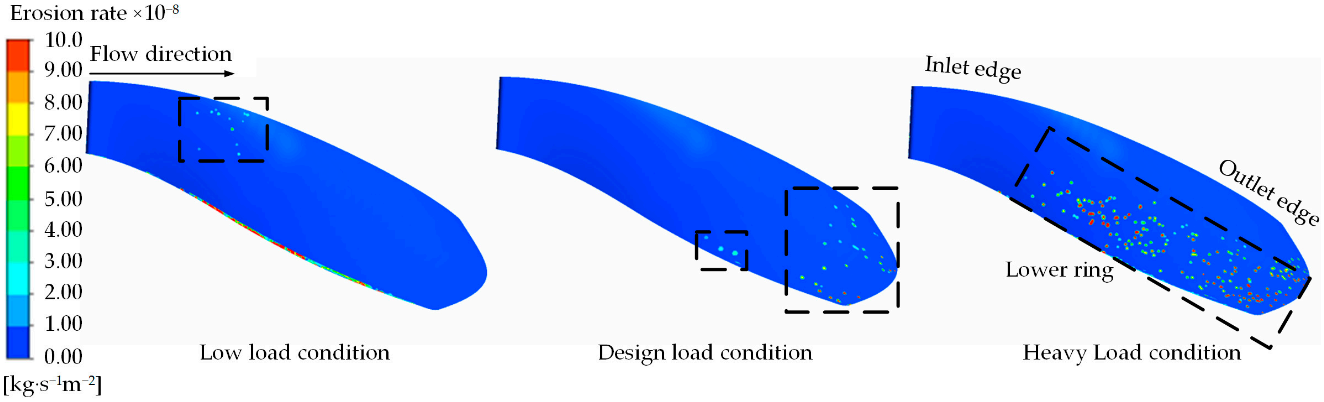

Figure 21. Sediment-induced wear distribution at the front of the runner's long blade.

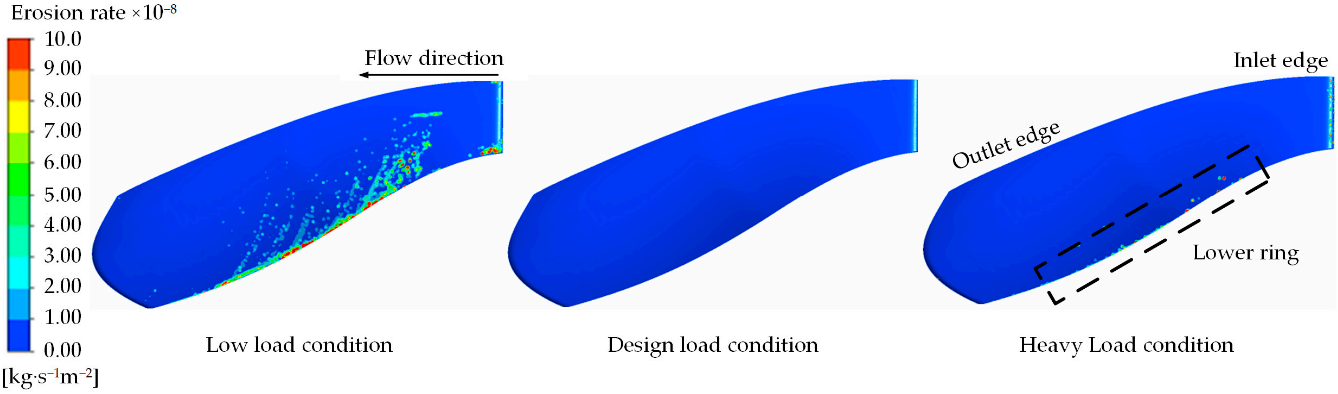

Figure 22. Sediment-induced wear distribution at the back of the runner's long blade.

(2) Wear analysis of the runner's short blade

As depicted in Figures 23 and 24, sediment distribution is primarily concentrated along the water outlet side of the front of the runner's short blade and near the lower ring at the bottom of the back of the blade. Under the low-load condition, sediment at the front of the runner's short blade is predominantly distributed along the edge of the lower blade ring, with no sediment deposition apparent in other areas. Regions with SVFs exceeding 0.0018 are primarily concentrated in the middle region of the back side of the short blade and near the bottom, close to the lower ring. Under the design load condition, areas with SVFs exceeding 0.0018 are mainly concentrated in the water outlet region at the front of the blade, while sediment deposition on the back is sparse, with volume fractions ranging between 0.0004 and 0.0006. Under the heavy-load condition, the sediment distribution is more concentrated, with areas having SVFs exceeding 0.0018 located primarily on the water outlet side of the front of the runner's short blade, near the bottom of the back side, and on the water inlet side.

Figures 25 and 26 illustrate the SVF curves on the surface of the active guide blade at 10% and 50% blade heights. Under the low-load condition, sediment deposition at the front of the runner's short blade is almost negligible, while the SVF at the back of the blade initially increases and subsequently decreases from the water inlet edge to the water outlet edge. The maximum SVF on the blade surface reaches approximately 0.3029. Under the design load condition, the SVF at the front of the runner's short blade gradually decreases from the water outlet edge to the water inlet edge. Meanwhile, on the back side of the runner's short blade, at the 50% blade height, the SVF first increases and then decreases from the water outlet edge to the water inlet edge, with the maximum SVF on the blade surface being approximately 0.0183. Under the heavy-load condition, the sediment distributions at the front and back of the runner's short blade at the 10% blade height exhibit no substantial changes. In particular, on the back side of the blade, the SVF exhibits a slight increase followed by a decrease from the water inlet edge to the water inlet edge. At 50% blade height, no sediment change is observed on the back, while the SVF at the front exhibits a gradual decline from the water outlet edge to the water inlet edge. The maximum SVF on the leaf surface reaches approximately 0.0213.

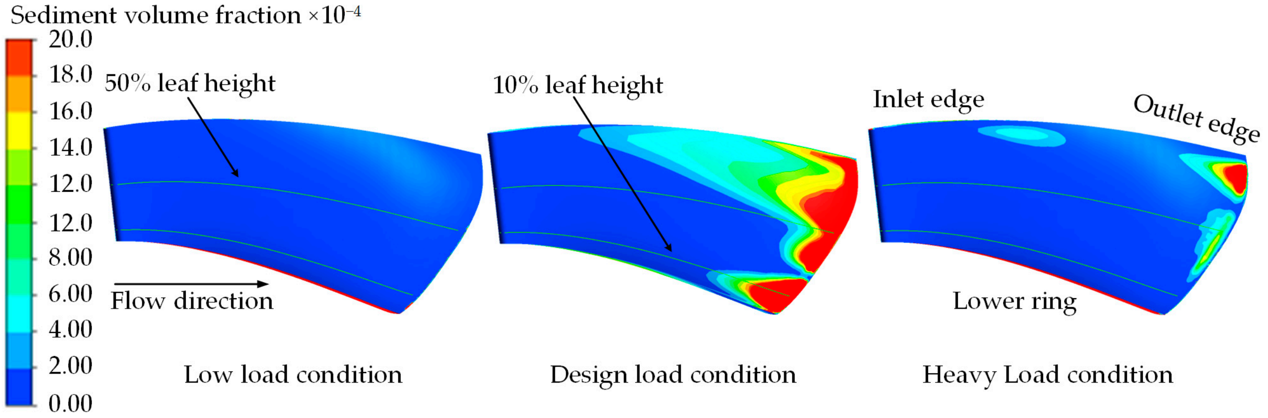

Figure 23. SVF at the front of the runner's short blade.

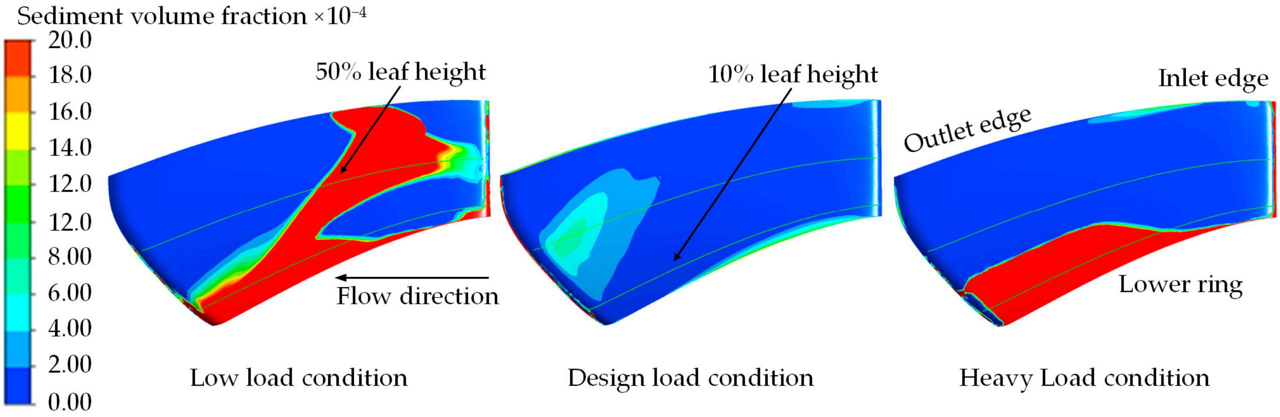

Figure 24. SVF at the back of the runner's short blade.

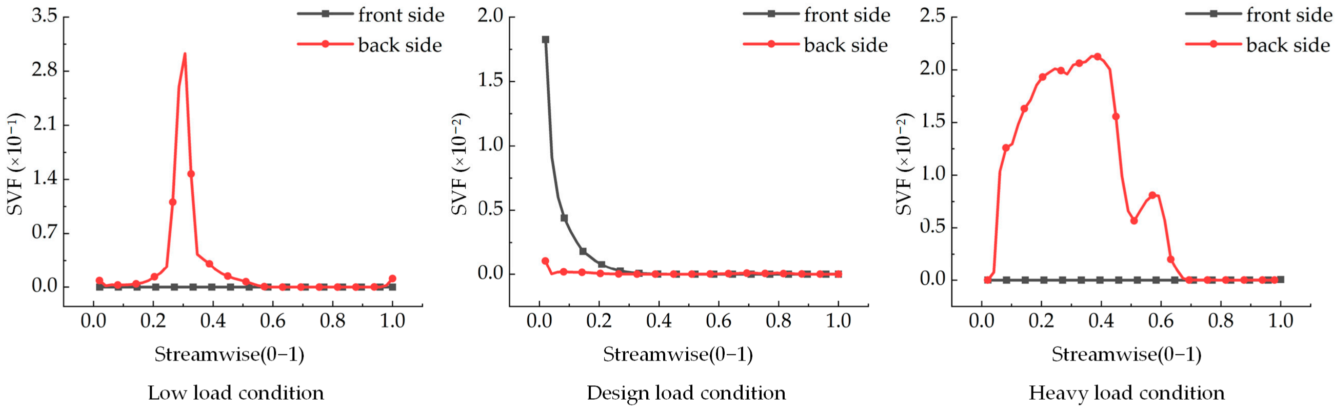

Figure 25. SVF on the surface of the runner's short blade at 10% blade height.

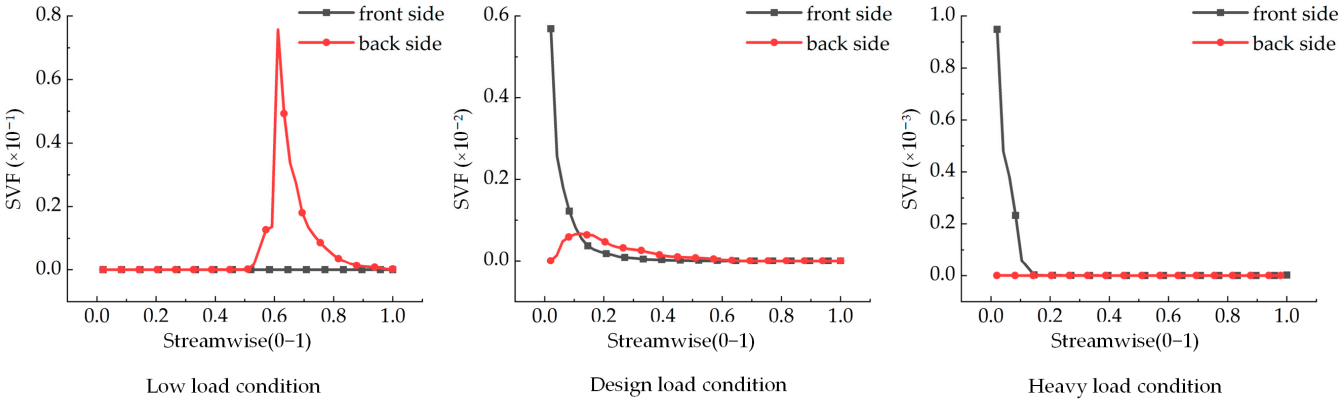

Figure 26. SVF on the surface of the runner's short blade at 50% blade height.

As illustrated in Figures 27 and 28, sediment-induced wear on the surface of the runner's short blade is minimal across all three working conditions and is primarily concentrated along the water edge of the blade and at its bottom near the lower ring. Under the low-load condition, some sediment-induced wear occurs near the water edge at the front of the runner's short blade, while at the back of the blade, sediment-induced wear is concentrated near the bottom of the blade. Regions with an erosion rate exceeding 9.0×10^{-8} kg·s^{-1}m^{-2} are primarily localized along the lower ring edge of the short blade. Under the design load condition, slight sediment-induced wear occurs at the front of the runner's short blade, while wear on the back is minimal and is primarily distributed along the edge of the lower ring. The erosion rate ranges from 3.0×10^{-8} to 6.0×10^{-8} kg·s^{-1}m^{-2}. Under heavy-load conditions, sediment-induced wear at the front of the runner's short blade is more widespread and exhibits a granular pattern, primarily near the water edge. Conversely, the sediment-induced wear at the back of the blade remains minimal and is primarily distributed near the water inlet and the lower ring of the water outlet. As illustrated in Figure 28, the degree of erosion on the blade surface is relatively significant under the low-load condition, and the influence of natural forces such as gravity on the sediment particles became more significant due to the low flow velocity and relatively large particle size (d = 0.27 mm), which prompted the sediment particles to undergo natural settling. The area resulting in the erosion rate exceeding 9.0×10^{-8} kg·s^{-1}m^{-2} is densely distributed on the surface at the bottom of the runner blade.

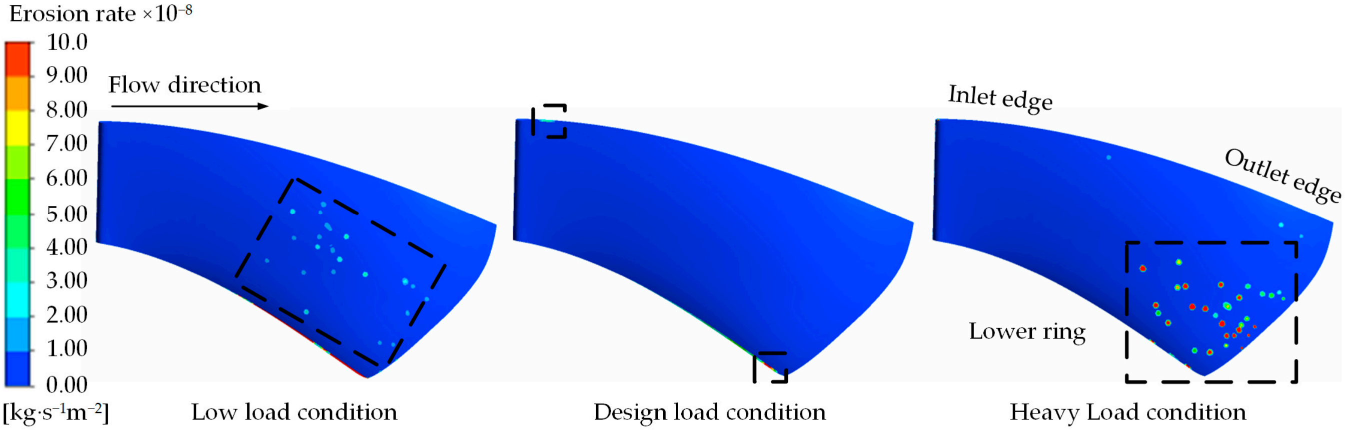

Figure 27. Sediment-induced wear distribution at the front of the runner's short blade.

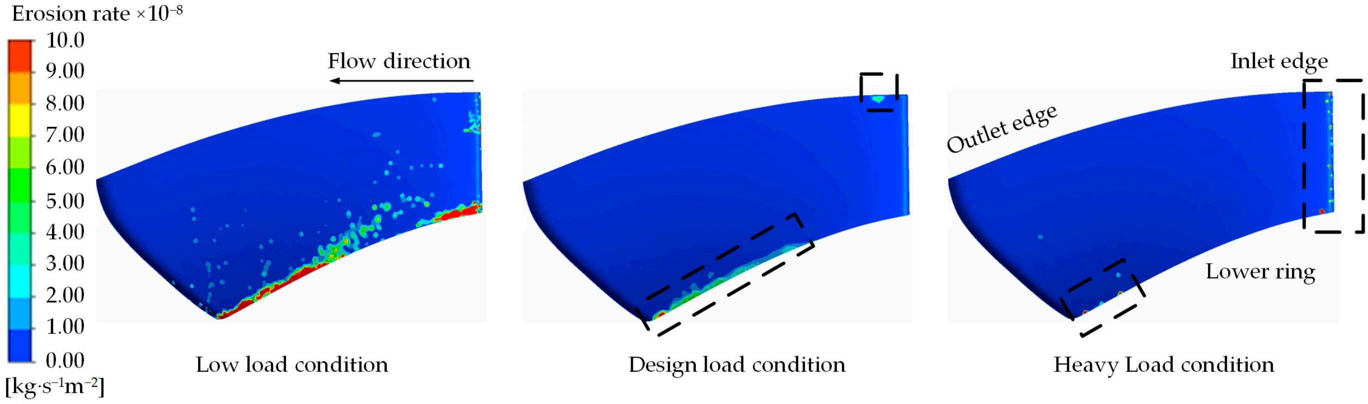

Figure 28. Sediment-induced wear distribution at the back of the runner's short blade.

5. Applicable Measures

Current research results and the accumulation of actual power station operation experience have provided some effective wear-resistant measures. These measures can, to a certain extent, reduce the hazards of hydroelectric power station sediment abrasion, prolong the working life of hydroelectric power station equipment in the sediment river, and improve its wear-resistant performance. The relevant measures are mainly applicable to the following four categories:

(1) Improve the sediment interception and drainage capacity of hydropower structures in hydropower stations.
(2) Improve the design of the hydraulic turbine to resist abrasion, including a reasonable selection of parameters of the hydraulic turbine model, and improvement of the hydraulic and structural design of the hydraulic turbine.
(3) Improve the manufacturing quality of hydraulic turbine components, including the processing quality of hydraulic turbine components, the selection of wear-resistant materials, and the spraying process.
(4) Reasonably arrange the operating conditions of hydraulic turbines and improve the maintenance measures of hydraulic turbines.

6. Conclusions

The sediment wear of the turbine overflow components was analyzed by comparing the sediment volume fraction and sediment wear distribution of the turbine overflow components under different operating conditions. The main conclusions are as follows:

(1) Under the three operating conditions, as the flow rate increases, the sediment distribution gradually expands. It spreads from the area near the lower ring of the stay vane to its tail region. For the guide vane, the sediment distribution gradually moves from near the disk to other regions. For the runner blade, sediment moves from the water edge near the lower ring to the water edge area of the blade. Overall, as discharge increases, the sediment distribution gradually shifts toward the edge of the blade, primarily concentrating in the head and tail regions of the guide vane and along the water edge area of the runner blade.
(2) Under the three working conditions, the surface of the stay vane exhibits almost no signs of sediment-induced wear, indicating minimal influence of sand–water flow. Sediment-induced wear on the surface of the guide vane is primarily concentrated in the head region and increases with increasing flow rate. Across the three working conditions, sediment-induced wear on the surface of the runner blade is primarily concentrated in the lower ring area, with the highest wear occurring under the low flow condition.
(3) The sediment-induced wear patterns on the stay vane, guide vane, and runner blade correspond to the distribution of SVFs. Under all three working conditions, wear on

the stay and guide vanes is primarily distributed in the head region of the stay and guide vanes, while the wear on the runner blade is primarily localized along the water edge and the bottom near the lower ring.

Author Contributions: Conceptualization, X.L.; Methodology, Z.Y.; Formal analysis, B.X. (Bing Xue); Investigation, B.X. (Bo Xu); Resources, Y.L. (Yongbo Li); Writing—original draft, K.X.; Writing—review & editing, Z.Z. and J.P.; Visualization, Z.T.; Supervision, J.P.; Project administration, B.Y.; Funding acquisition, Y.L. (Youping Li). All authors have read and agreed to the published version of the manuscript.

Funding: The research was supported by the National Natural Science Foundation of China Regional Innovation and Development Joint Fund project "Air doping erosion reduction mechanism and control of cavitation wear coupling damage of pump turbine in high altitude area" (No: U23A20669).

Data Availability Statement: Data is contained within the article.

Acknowledgments: This project was funded by China Yangtze Power Co., Ltd. (Contract No. Z152302056).

Conflicts of Interest: This study is a collaborative effort between Xihua University and China Yangtze Power Co., Ltd. The authors declare that the research was conducted in the absence of any commercial or financial relationships.

References

1. Flores, E.; Bornard, L.; Tomas, L.; Liu, J.; Couston, M. Design of large Francis turbine using optimal methods. *IOP Conf. Ser. Earth Environ. Sci.* **2012**, *15*, 022023. [CrossRef]
2. Pang, J.; Liu, H.; Liu, X.; Yang, H.; Peng, Y.; Zeng, Y.; Yu, Z. Study on sediment erosion of high head Francis turbine runner in Minjiang River basin. *Renew. Energy* **2022**, *192*, 849–858. [CrossRef]
3. Liu, X. Studies of Solid-liquid Two-phase Turbulent Flows and Wear in Hydraulic Turbomachinery. *Chin. J. Hydrodyn.* **1996**, *11*, 606–609.
4. Pan, J.; Liu, Q.; Pang, J.; Zhang, F.; Tao, R.; Xiao, R.; Zhou, L.; Liu, W. Comparative evaluation of sand erosion in reversible turbine at pump mode and turbine mode. *J. Energy Storage* **2024**, *79*, 110185. [CrossRef]
5. Huang, J.; Zhang, L.; Yao, J.; Long, L. Numerical simulation of two-phase turbulent flow in Francis turbine passage on sediment erosion. *J. Drain. Irrig. Mach. Eng.* **2016**, *34*, 145–150.
6. Wang, J. Study on Cavitation Characteristics of Mixed-Flow Turbine Under Sediment-Laden Water Flow. Master's Thesis, Zhejiang University, Hangzhou, China, 2016.
7. Zhang, L.; Cao, Z.; Wang, J.; Wang, S.; Yang, Z.; Shi, G. Numerical Simulation of Wear of the Guide vane of Turbine in Sediment-laden River. *J. Hydraul. Archit. Eng.* **2022**, *20*, 1–7.
8. Xu, J.; Chen, S.; Shen, J.; Wu, Z.; Qian, Z.; Zhou, X. Research on Numerical Simulation and Wear Characteristics of Axial Flow Pump Based on Particle Model. *Shaanxi Water Resour.* **2021**, 1–4+7. [CrossRef]
9. Liu, J.; Pang, J.; Liu, X.; Huang, Y.; Deng, H. Analysis of Sediment and Water Flow and Erosion Characteristics of Large Pelton Turbine Injector. *Processes* **2023**, *11*, 1011. [CrossRef]
10. Hu, Q.; Liu, X.; Zhao, Q. Numerical Simulation of Sand Erosion of Francis Turbine Runner Based on Two-phase Flow Theory. *Water Resour. Power* **2016**, *34*, 183–186.
11. Wang, H.; Pang, J.; Liu, X.; Zhou, Z.; Gang, Y.; Lai, Z.; Wang, J.; Qin, B. Analysis on cause of erosion of guide vane of high-head Francis turbine in sandy river. *Energy Sci. Eng.* **2024**, *12*, 3704–3717. [CrossRef]
12. Li, S.; Yao, B.; Pang, J.; Liu, D.; Chengmei, D.; Jiang, D.; Wang, H.; Gang, Y.; Cheng, H.; Liu, X. Research on the technical improvement of the turbine runner of a power station based on improving stability. *Energy Sci. Eng.* **2024**, 1–16. [CrossRef]
13. Li, Y.; Zhu, Y.; Xiao, Y.; Liu, J.; Liang, Q.; Li, H. Numerical analysis of bucket hydro-abrasive erosion in Pelton turbine in sediment season. *J. Hydroelectr. Eng.* **2024**, *43*, 15–22.
14. Jia, L.; Zeng, Y.; Liu, X.; Huang, W. Numerical Simulation and Experimental Study on Sediment Wear of Stay vanes of Hydraulic Turbines in Muddy River Based on Discrete Phase Model. *Processes* **2023**, *11*, 2117. [CrossRef]
15. Yao, B.; Li, J.; Zhao, T.; Liu, X. Sediment wear prediction model of ZG06Cr13Ni4Mo turbine guide vane in sediment-laden hydropower station. *Mater. Express* **2021**, *11*, 1866–1873. [CrossRef]
16. Wang, L.; Li, B.; Zhao, W. Dynamics and Wear Analysis of Hydraulic Turbines in Solid-liquid Two-phase Flow. *Open Phys.* **2019**, *17*, 790–796. [CrossRef]
17. Koirala, R.; Thapa, B.; Neopane, H.P.; Zhu, B.; Chhetry, B. Sediment erosion in guide vanes of Francis turbine: A case study of Kaligandaki Hydropower Plant, Nepal. *Wear* **2016**, *362–363*, 53–60. [CrossRef]
18. Huang, Y.; Deng, F.; Deng, H.; Qing, Q.; Qin, M.; Liu, J.; Yu, Z.; Pang, J.; Liu, X. Study on Internal Flow Characteristics and Abrasive Wear of Pelton Turbine in Sand Laden Water. *Processes* **2023**, *11*, 1570. [CrossRef]

19. Pan, J.; Ma, J.; Han, J.; Zhou, Y.; Wu, L.; Zhang, W. Prediction of sediment wear of francis turbine with high head and high sediment content. *Front. Energy Res.* **2023**, *10*, 1117606. [CrossRef]
20. Pang, J.; Chang, X.; Gang, Y.; Zhou, Z.; Xiang, W.; Zhou, L.; Liu, X.; Wang, Z. Design and Study of a Sediment Erosion Test Device for a Single-Flow Channel in the Guide Apparatus of a Reaction Hydraulic Turbine. *J. Mar. Sci. Eng.* **2024**, *12*, 777. [CrossRef]
21. Zhang, L.; Cao, Z.; Wang, J.; Wang, S.; Yang, Z.; Shi, G. Study on influence of operating conditions on turbine vane wear in sandy river. *Water Resour. Hydropower Eng.* **2022**, *53*, 148–156.
22. Yang, H.; Liu, X.; Tian, W.; Pang, J.; Xu, L. Sediment Abrasion of Turbine Guide Vanes at Xiate Hydropower Station in Xinjiang. *J. Chin. Soc. Power Eng.* **2022**, *42*, 190–196.
23. Wang, J.; Song, X.; Wang, H.; Tao, R.; Wang, Z. Numerical prediction of erosion of Francis turbine in sediment-laden flow under different heads. *Processes* **2023**, *11*, 2523. [CrossRef]
24. Rajan, G.K.; Cimbala, J.M. Computational and theoretical analyses of the precessing vortex rope in a simplified draft tube of a scaled model of a Francis turbine. *ASME J. Fluids Eng.* **2017**, *139*, 021102. [CrossRef]
25. Yang, J.; Peng, C.; Li, C.; Liu, X.; Liu, J.; Wang, Z. Design and verification of Francis turbine working in sand laden hydro-power plant. *Renew. Energy* **2023**, *207*, 40–46. [CrossRef]
26. Xu, T.; Cheng, Q.; Lin, C.; Yu, Q.; Hu, X. Study on Flow Characteristics of Francis Turbine Based on Large-Eddy Simulation. *Water* **2023**, *15*, 3372. [CrossRef]
27. Pang, J.; Yao, B.; Liu, X.; Li, J.; Xiao, M.; Jiang, D.; Tang, W.; Zhou, L.; Lai, Z. Influence of guide vane opening on channel vortex and pressure pulsation in Francis turbine runners. *Phys. Fluids* **2024**, *36*, 043325. [CrossRef]
28. Liang, A.; Li, H.; Zhang, W.; Yao, Z.; Zhu, B.; Wang, F. Study on pressure fluctuation and rotating stall characteristics in the vaneless space of a pump-turbine in pump mode. *J. Energy Storage* **2024**, *94*, 112385. [CrossRef]
29. Hu, L.; Liang, A.; Li, H.; Zhang, W.; Zhu, B. Impact of rotor-stator axial spacing on the gas-liquid-solid flow characteristics of a multiphase rotodynamic pump based on the Euler multi-fluid model. *Phys. Fluids* **2024**, *36*, 063314. [CrossRef]
30. Bajracharya, T.R.; Acharya, B.; Joshi, C.B.; Saini, R.; Dahlhaug, O.G. Sand erosion of Pelton turbine nozzles and buckets: A case study of Chilime Hydropower Plant. *Wear* **2008**, *264*, 177–184. [CrossRef]
31. Pang, J.; Liu, H.; Liu, X.; Ren, M.; Zhang, P.; Yu, Z. Analysis on the escape phenomenon of oil mist from turbine lower guide bearing based on VOF model. *Adv. Mech. Eng.* **2021**, *13*, 16878140211060929. [CrossRef]